Graphene-based anisotropic polarization meta-filter

Cheng Zhang [a],*, Chang Long [b], Sheng Yin [b], Rong Guo Song [a,c], Bo Han Zhang [a,c], Jing Wei Zhang [a], Da Ping He [a,d],*, Qiang Cheng [e],*

[a] Hubei Engineering Research Center of RF-Microwave Technology and Application, School of Science, Wuhan University of Technology, Wuhan 430070, China
[b] Aerospace Science and Industry Wuhan Magnetism-Electron Co. LTD, Wuhan 430080, China
[c] School of Information Engineering, Wuhan University of Technology, Wuhan 430070, China
[d] State Key Laboratory of Advanced Technology for Materials Synthesis and Processing, Wuhan University of Technology, Wuhan 430070, China
[e] Department of Radio Engineering, State Key Laboratory of Millimeter Waves, Southeast University, Nanjing 210096, China

HIGHLIGHTS

- Graphene film with arbitrary sheet resistance is fabricated and characterized for flexibly design of electronics.
- A graphene-based anisotropic meta-filter is proposed to select and manipulate the valuable polarization without redundant reflection.
- The proposed meta-filter shows a wideband characteristic beyond the X band.

GRAPHICAL ABSTRACT
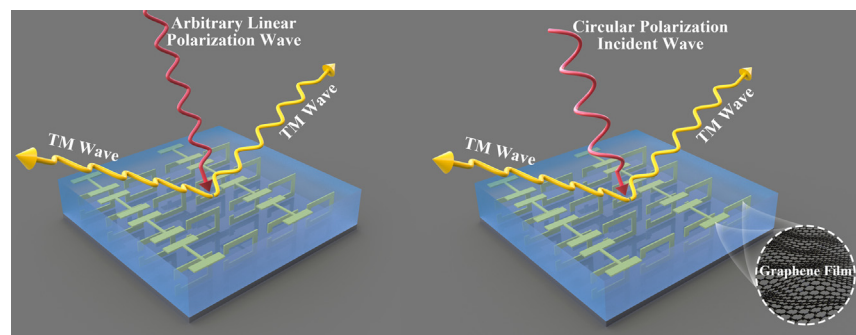
ARTICLE INFO

ABSTRACT

Artificially engineered metamaterials/metasurfaces provide an extraordinary strategy for tailoring the electromagnetic properties of devices, which may break conventional limits in existing polarization filters. Hence, this paper presents an anisotropic graphene-based meta-filter that contains the features of both a phase-gradient metasurface and an electromagnetic absorber, thereby enabling versatile beam behaviors and low reflection loss under orthogonal polarization. In the meantime, our design offers an idealized platform for polarization decomposition and manipulation. Three cases are presented to assess the performance of the proposed meta-filter in the microwave band of interest and to demonstrate its anisotropic nature and polarization-extraction functionality. The corresponding meta-filters are meanwhile characterized by numerical simulation and experimental measurement, the results of which are in good agreement. In addition, the employment of novel graphene films endows the bi-functional meta-filter a promising candidate for future electronic applications in special scenarios calling for excellent environmental resistance and superb flexibility et al.

1. Introduction

The flourishing development of wireless techniques, particularly fifth- and even sixth-generation networks, Internet of Things, or artificial intelligence, provides us with a convenient and intelligent life [1]. With these developments, the spectral efficiency and system capacity needed are ever-increasingly than

* Corresponding authors at: Hubei Engineering Research Center of RF-Microwave Technology and Application, School of Science, Wuhan University of Technology, Wuhan 430070, China (C. Zhang).
E-mail addresses: czhang2020@whut.edu.cn (C. Zhang), hedaping@whut.edu.cn (D.P. He), qiangcheng@seu.edu.cn (Q. Cheng).

before, and therefore polarization is multiplex-used to expand the capacity of the network [2], resulting in a significant requirement for polarization filtering and modulation. Besides, purity polarization control is also meaningful in many areas of scientific research, including astronomy, chemistry, and biology [3–4].

Standard approaches for isolating a specific polarization involve the adoption of a grating [5–6], a waveguide [7], or a photonic crystal fiber (PCF) [8–10] to select the required incoming polarized waves. However, these methods have several drawbacks that limit their practical applications. For example, the polarization state of interest can be feasibly selected by utilizing the traditional grating or waveguide, but non-loss reflection occurs with regard to the needless part. Thus, untreated extra electromagnetic (EM) energy can cause EM interference in electronics disturbing their regular operation. For PCFs being widely used in the terahertz, infrared, and visible light regions, redundant polarization can be dissipated due to its high loss property, and excellent polarization isolation is simultaneously achieved once surface plasmon polariton (SPP) modes are evoked. Although PCFs have been significantly improved, they are rarely implemented in the microwave domain. Hence, in analogy with PCF, spoof SPPs [11–13] are introduced to create a band-pass filter within broadband, but the unique feeding method makes a barrier for its development as well as the polarization-sensitive characteristic. Needless to say, relevant researches mainly focus on selecting the desired polarization, whereas its post-manipulation is still lack of research. Additionally, the treatment of superfluous portions is also urgently needed to avoid secondary EM pollution.

Recently, there has been increasing interest in metamaterial/metasurface [14–17], comprising sub-wavelength artificial unit cells. With the appropriate design of the meta-atoms and optimization of the aperture, some fascinating phenomena can be successfully achieved such as holographic image [18–19], carpet cloaking [20–21], EM black hole [22–23], and anomalous reflection/transmission [24–25], paving the way for dealing with the problems mentioned above. For instance, anisotropic metasurfaces enable robust control of differently polarized EM waves [26–27]. However, only non-loss random diffusion can be used to suppress the backward scattering of redundant polarization.

Due to their omnidirectional features, plenty of new EM radiation sources are generated, leading to severe EM compatibility problems. As an alternative scheme for restricting backward reflection, metamaterial absorbers can get rid of this limitation through dissipating the incident waves instead of scattering [28–30]. For example, multilayered metallic-dielectric quadrangular frustum pyramids were put forward to realize a total absorption of the incident wave over an ultra-wide spectral band [31]. Unfortunately, it may not be a proper solution due to the non-selectivity suppressing of arbitrarily polarized waves, giving rise to the inevitable loss of partial carried-information. While several absorbers that react only with limited polarized incidences have been developed and investigated [32–34], manipulation of the residual fields is rarely reported.

Inspired by the previous work, we raise a bold hypothesis: Is it possible to build a meta-filter integrating the benefits of both microwave metamaterial absorbers and diffusion metasurfaces? Once achieved, the required polarized waves can be smoothly controlled by modulating the phase-gradient surface [35–36], and the surplus polarized energy can be absorbed and consumed through ohmic loss [37–38] or dielectric loss [39]. Besides, as a remarkable delegation of novel conductive material, there are ongoing researches to discover the physical or chemical features of graphene [40]. In particular, graphene film offers unique advantages, including tunable conductivity over an extensive range, high-temperature resistance, and flexibility et al. and shows enormous potential for addressing the aggravating EM problem. To date, it has been used in the investigation of antennas [41], energy harvester [42], filters [43], and radio-frequency identification (RFID) technology [44–45] et al., due to its mechanical properties being superior to those of metal materials. Therefore, our assumption can be promoted to a high level of real-life applications by implanting the graphene film instead of traditional metal and other semiconductor materials [46].

Herein, a graphene-based bi-functional metasurface (Fig. 1 (a − b)) is designed for the first time of our best knowledge, to realize the treatment of EM pollution with the simultaneous manipulation of scattering behaviors, such as beam steering and the multiple beams of valuable polarizations. When radiated by TE plane waves,
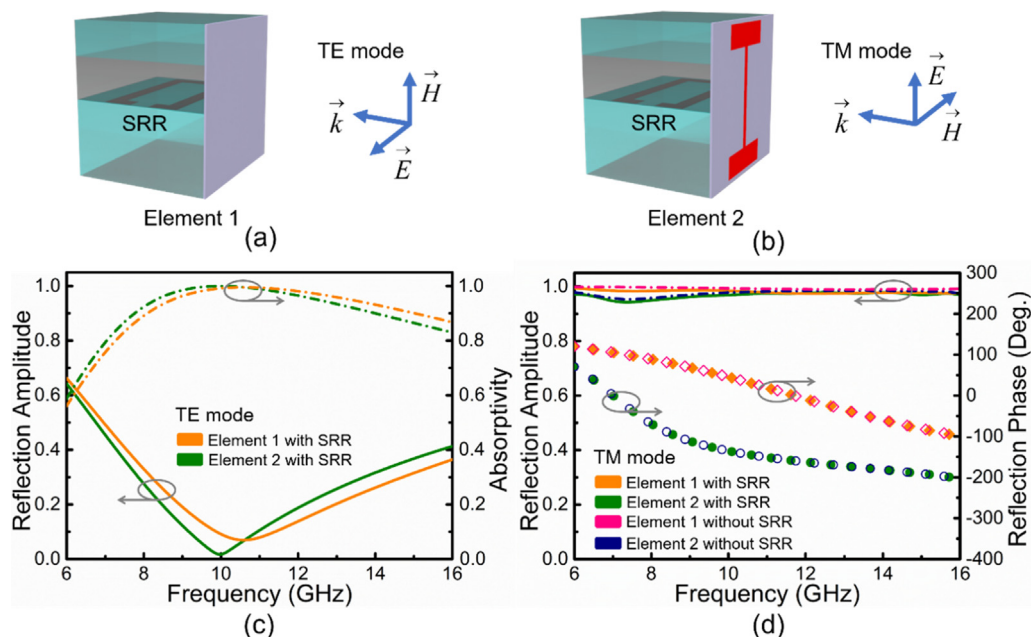

Fig. 1. Schematics of the proposed Element 1 (a) and Element 2 (b). Inset: Illustrations of the incident waves. Reflection response of the typical unit cells under the illumination of plane waves with TE (c) and TM (d) modes.

EM energy is only dissipated by the meta-filter due to the ohmic loss (Fig. 1(c)). In contrast, the reflected profiles of the incident TM waves can be adjusted arbitrarily by predesigning the distribution of two anti-phase meta-atoms across the aperture of the meta-filter (Fig. 1(d)) [47]. These dual functions can be performed beyond the X band (from 8.0 GHz to 12.4 GHz), showing considerable potential for practical applications. In addition, our design provides another fantastic function, namely polarization decomposition, whereby the TM component can be extracted from the total incident linear- or circular-polarized fields with the help of our strategy, as well as flexibly modulated. In the meantime, because of the excellent attenuation of TE aspect, the proposed meta-filter does a noble favor in certain particular application scenarios calling for excellent cross-polarization isolation and high-purity single polarization.

2. Theory and design

2.1. Unit cell design

To realize the abovementioned two functions within one meta-filter, unit cells are proposed, as depicted in Fig. 1(a − b), with their corresponding geometry and size optimized through numerical simulation. Aiming at easy design and implementation, two elements with π phase difference are introduced to simultaneously control the spatial patterns of the selected polarization and eliminate the orthogonal polarization. A sandwich structure is typically optimal for bi-functional meta-atoms (Fig. 1(a − b)), with the top layer of Element 1 being a non-shaped substrate, and Element 2 having an I-shape. In both elements, the middle layer consists of arrayed graphene-based split-ring resonators (SRRs) (with a sheet resistance of 35 $\Omega/\square$) embedded in an F4B dielectric matrix (permittivity: 2.65 + i0.001) backed by a graphene ground plane. Both the I-shaped structure and ground layer consist of high-conductivity graphene film, the sheet resistance of which may reach 0.03 $\Omega/\square$. The detailed structural parameters of the basic unit cells are provided in **Supplementary Note S1**.

As shown in Fig. 1(c), our designs absorb more than 90% of TE waves from 8.0 GHz to 14.2 GHz. With respect to orthogonally polarized incident waves (Fig. 1(d)), identical reflection amplitude but opposite phase states (with a phase difference of 180° ± 30°) can be achieved between the two elements from 7.5 GHz to 12.4 GHz, facilitating to arbitrary control of the spatial EM waves. (See **Supplementary Note S2 for a detailed description of the simulation method**).

To explore the anisotropic performance of the proposed meta-atoms, the transmission line (TL) theory is adopted [48]. With regard to the TE case (Fig. 1(c)), the typical unit cells (Element 1 and Element 2) behave as simple TL models illustrated in Fig. 2 (a). Notably, the graphene ground layer is equivalent to a short-circuit TL owing to its high conductivity. To reveal why the two different elements show similar and stable absorption performance, we first define the middle layer of the designed unit cell as a black box, of which the characteristic parameters are not cared about here. For the same structural intermediate layers, the black box for Element 1 is identical to that for Element 2. From Fig. 2(a), it can be easily determined that the input impedance (Z_{in}^{TE}) of the meta-structure is the total impedance of the parallel connection between the surface impedance (Z_s^{TE}) of the top layer and the black box. Thus Z_{in}^{TE} is determined by Z_s^{TE} obtained using the following relation [49]:

$$Z_s^{TE} = \frac{Z_0 S_{21}}{1 - 2S_{21}} \text{ and } Z_0^{TE} = Z_0/\cos\theta, \tag{1}$$

where Z_0 is the wave impedance of the free space, θ is the incident angle, and S_{21} represents the transmission coefficient. Hence, by substituting the corresponding S-parameters (Fig. 2(b)) into Eq. (1), nearly identical Z_s^{TE} values are obtained for Elements 1 and 2, approving that $Z_{in,Element1}^{TE}$ is approximately equal to $Z_{in,Element2}^{TE}$. Once Z_{in}^{TE} has been derived, the reflection coefficients (R) of the essential cells can be computed according to the following TL relations:

$$R = \frac{Z_{in}^{TE/TM} - Z_0^{TE/TM}}{Z_{in}^{TE/TM} + Z_0^{TE/TM}}, \tag{2}$$

in which $Z_0^{TM} = Z_0\cos\theta$. Based on the previous analysis and Eq. (2), similar reflection coefficients for Elements 1 and 2 are determined,
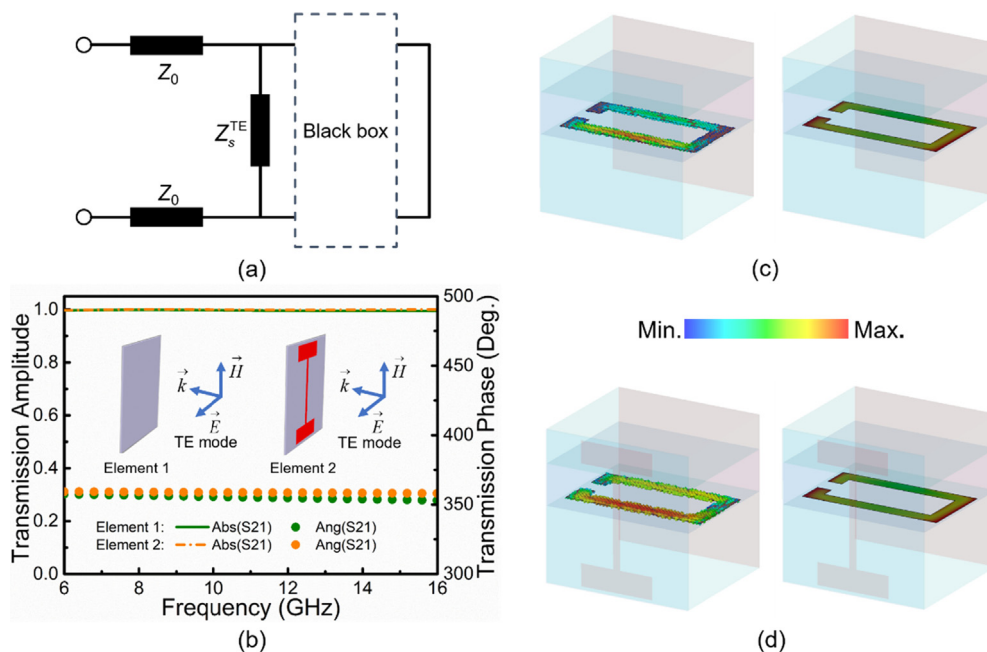

Fig. 2. Equivalent TL of the proposed meta-atoms (a − b) for TE mode incident waves. (b) Reflection characteristics of the upper structure of typical particles. Simulated surface currents and power-loss densities of the graphene-built SRRs: (c) Element 1 at 10.5 GHz; (d) Element 2 at 10 GHz.

which is consistent with the simulated predictions (Fig. 1(c)). To further identify the source of EM absorption, the simulated surface currents and power-loss densities of the graphene-built SRRs at resonance frequencies are presented in Fig. 2(c − d). It is worthy to note that the strong absorption at 10.5 GHz (Element 1) originates from electric resonances driven by the incident waves, since the currents are tightly localized at the middle SRRs (left-side image of Fig. 2(c)). The EM power can be dramatically dissipated in areas where currents accumulate (right-side image of Fig. 2(c)), because the surface currents lead to significant ohmic loss at the meta-filter with $P_{loss} = I^2R$, in which R is the surface resistance. A similar phenomenon at 10 GHz (Element 2) is also readily observed in Fig. 2 (d), despite the different current intensities. Besides, the absorption efficiency is also theoretically analyzed. Due to the high ohmic resistance of the graphene-based SRRs, the Q factor sharply declines when interacting with the incident waves, giving rise to a broadband performance shown in Fig. 1(c).

In the following, to uncover TM wave manipulation mechanism, Elements 1 and 2 are modeled as the corresponding TL models shown in Fig. 3(a − b). As such, the ABCD matrix for the TM case can be written as

$$\begin{bmatrix} A & B \\ C & D \end{bmatrix}_{Element1} = \begin{bmatrix} \cos k_r d & jZ_r \sin k_r d \\ j\frac{\sin k_r d}{Z_r} & \cos k_r d \end{bmatrix}, \text{ and} \tag{3}$$

$$\begin{aligned} \begin{bmatrix} A & B \\ C & D \end{bmatrix}_{Element2} &= \begin{bmatrix} 1 & 0 \\ Z_s^{TM} & 1 \end{bmatrix}\begin{bmatrix} \cos k_r d & jZ_r \sin k_r d \\ j\frac{\sin k_r d}{Z_r} & \cos k_r d \end{bmatrix} \\ &= \begin{bmatrix} \cos k_r d & jZ_r \sin k_r d \\ Z_s^{TM}\cos k_r d + j\frac{\sin k_r d}{Z_r} & jZ_s^{TM}Z_r \sin k_r d + \cos\beta_r d \end{bmatrix}, \end{aligned} \tag{4}$$

where Z_s^{TM} is the surface impedance of the top particle; d, Z_r and k_r are the thickness, characteristic impedance, and the wavenumber of the substrate, respectively. Based on the TL theory, the input impedance can be calculated as

$$Z_{in}^{TM} = \frac{AZ_l + B}{CZ_l + D}, \tag{5}$$

in which Z_l represents the load impedance. Due to the ultra-low sheet resistance of backed graphene film (0.03 $\Omega/\square$), Z_l in our design can be regarded as 0. Therefore, Eq. (5) can be simplified as

$$Z_{in}^{TM} = \frac{B}{D}. \tag{6}$$

By substituting Eqs. (3) and (4) into Eq. (6), the input impedance of Elements 1 and 2 can be given as

$$Z_{in,Element1}^{TM} = jZ_r \tan k_r d, \text{ and} \tag{7}$$

$$Z_{in,Element2}^{TM} = \frac{jZ_r \tan k_r d}{1 + jZ_s^{TM}Z_r \tan k_r d}. \tag{8}$$

Comparing Eq. (7) and Eq. (8) shows that Z_s^{TM} is the only factor that determines the different reflection responses between Elements 1 and 2, based on Eq. (2). Thus, if we defined Element 1 as the initial reflection state, its phase difference with respect to Element 2 can be flexibly tuned by changing Z_s^{TM} that is directly related to the geometric structure of the top particle in Element 2. According to the relevant research mentioned above, the I-shaped pattern can be successfully selected by sweeping the structural parameters with the commercial software — CST microwave studio 2019. Furthermore, the resonant feature of the predesigned meta-atoms is simultaneously invoked to explain the physical mechanism. The simulated E-field distributions concerning Element 1 (Fig. 1(a)) and Element 2 (Fig. 1(b)) are provided in Fig. 3(c − d), respectively, at the frequencies with 0 phase response. For Element 1 illuminated with TM waves at 12 GHz, the E-field is barely coupled to the top layer and middle SRRs (Fig. 3(c)), resulting in the ultra-low reflection loss (Fig. 1(d)). For Element 2, however, the top I-shaped structure can be regarded as an equivalent circuit model (inset of Fig. 3 (d)), of which the resonance is driven by an incident wave at $f_r = \frac{1}{2\pi\sqrt{LC}}$ [49]. Due to the LC resonance at 7 GHz, the E-field localized near the two arms can be dramatically driven (Fig. 3(d)) to induce the reflection phase shift. In the meantime, similar to Element 1, little E-field can be observed on the graphene-based SRRs
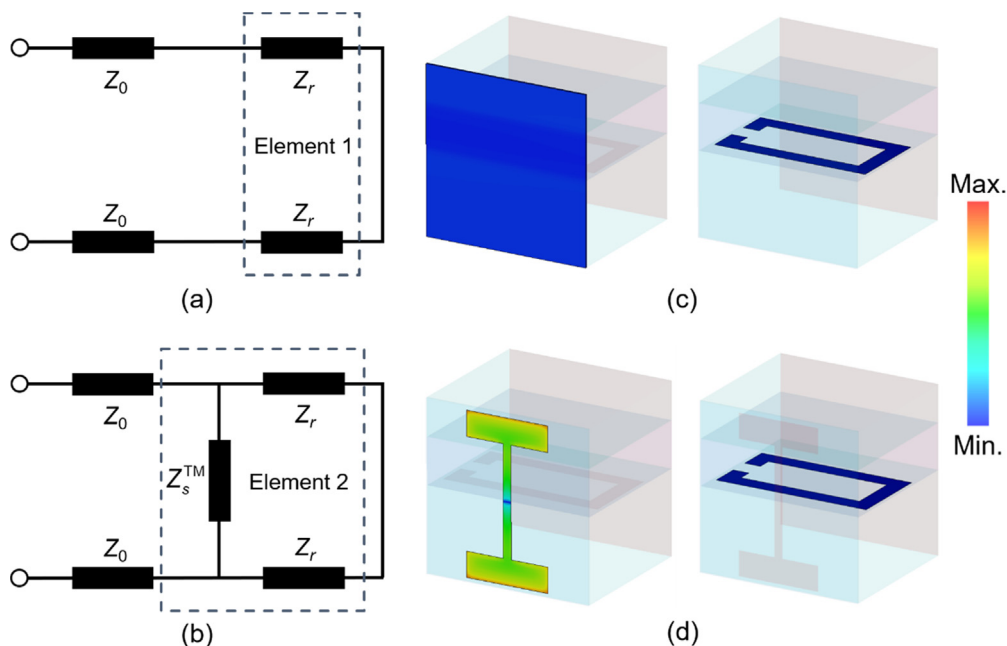

Fig. 3. Equivalent TL of the proposed meta-atoms (a − b) for TM mode incident waves. Simulated E-field distributions: (c) Element 1 at 12 GHz; (d) Element 2 at 7 GHz. Inset of (d): equivalent circuit model of the top I-shaped structure.

with relatively high sheet resistance (35 Ω/□), thus achieving low input loss as previously predicted in Fig. 1(d).

2.2. Aperture design

To evaluate the performance of the proposed meta-filter, an example is presented to illustrate the polarization-dependent functionality. This demonstrates that the required polarization can be selected and manipulated, while simultaneously eliminating the surplus polarization. During the full-wave simulation, a block of 8 × 8 identical elements is employed as the basic supercell of the meta-filter, to mimic the periodic boundary condition for the composing meta-atoms.

With regard to Case 1 shown in Fig. 4, a pseudorandom distribution of typical unit cells is preset to realize broadband random diffusion of the reflected TM waves based on the generalized Sell's law [50] that favors anomalous scattering. In the meantime, the TE waves can be dissipated due to the absorption feature of the proposed meta-atoms (Fig. 1(c)). To demonstrate the above phenomena, the simulated three-dimensional (3D) scattering patterns of the meta-filter with the predesigned aperture are obtained. For comparison, the 3D scattering patterns of a same-sized metallic plate are also supplied. In Fig. 4(a − c), it can be seen that a dramatic reduction in the main beam is achieved under illumination from TE plane waves at 9 GHz, 10 GHz, and 11 GHz, in contrast to that of the metallic plate (Fig. 4(g − i)). Besides, by comparing the second column (Fig. 4(d − f)) with the third column (Fig. 4 (g − i)), it is easy to find that the rough surface enables the backward reflection waves of the TM mode to be sharply suppressed, via omnidirectional deflection of the incoming EM energy to the upper space. Eventually, the broadband performances of our design are also revealed in Fig. 4(j − k), and its excellent ability to reduce the radar cross-section (RCS) by more than 10 dB is evident at almost the same operating frequency band (8 GHz to 14 GHz) for both normal incident TE (Fig. 4(j)) and TM (Fig. 4(k)) waves. To be noted that because of the edge scattering effect, the effective working frequency band (where the RCS reduction is more than 10 dB) of the array under normal TE waves (Fig. 4(j)) is slightly improved in contrast to that of the unit cells in Fig. 1(c), where the absorptivity is greater than 90%.

Case 1 confirms that, as expected, echo-free polarization filtering and manipulation can be conducted in a wide bandwidth. This capability also offers a new route for the decomposition and modulation of incoming waves, such as linear- and circular-polarized waves. Another two cases (Figs. 5 and 6) are presented to demonstrate this feature.

In Case 2 shown in Fig. 5, the predesigned meta-filter is used to split a normal linear-polarized incident wave into two orthometric components (TE and TM parts). The corresponding E-field vector travels along the diagonal direction (Fig. 5(a) and 5(d)). The first, second, and third columns in Fig. 5 represent the total, TM part and TE part 3D scattering patterns at 10 GHz, respectively. When different unit cells are arranged as an interval distribution (Fig. 5 (a − c)), a two-beam spatial pattern is generated in the total far field as shown in Fig. 5(a). Similar two-beam splitting in terms of TM component can be successfully extracted with little
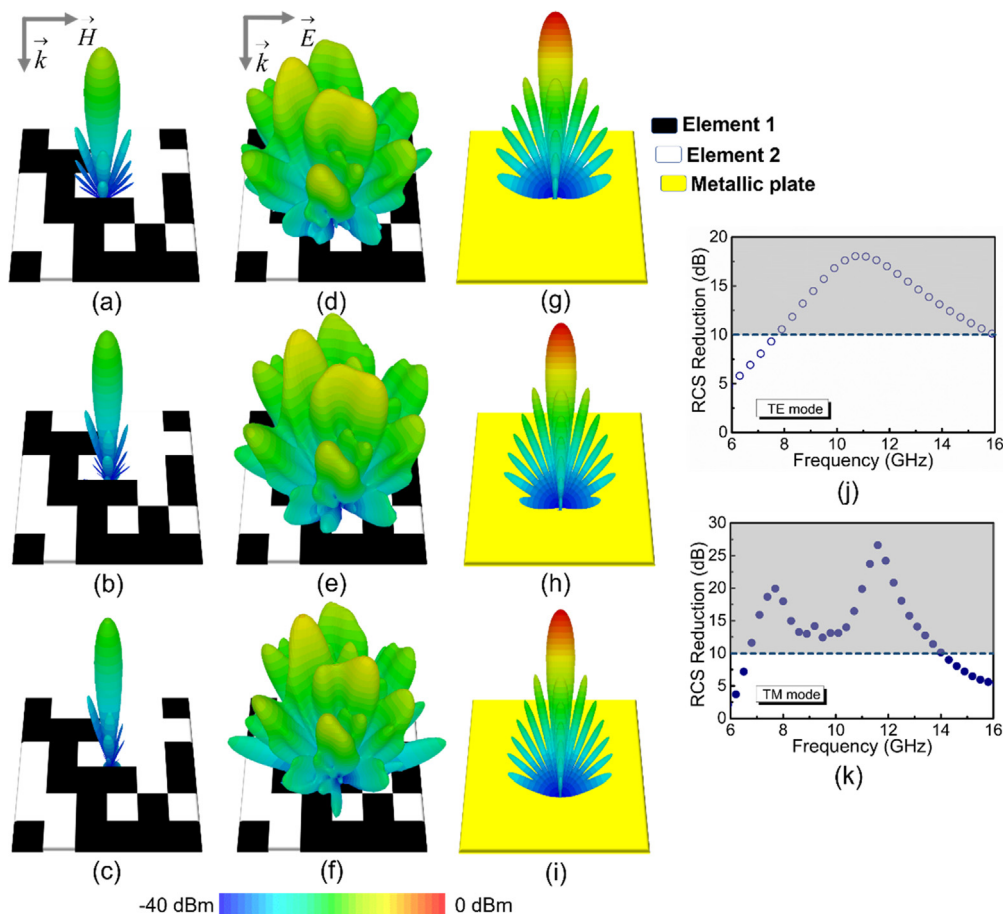

Fig. 4. Simulated 3D scattering patterns of the proposed meta-filter with the incidence of the TE (a − c) and TM (d − f) plane waves at 9 GHz (a, d), 10 GHz (b, e) and 11 GHz (c, f), respectively. (h − i) Simulated 3D scattering patterns of the same-sized metallic plate. RCS reduction of the predesigned bi-functional meta-filter versus frequency for TE mode (j) and TM mode (k).
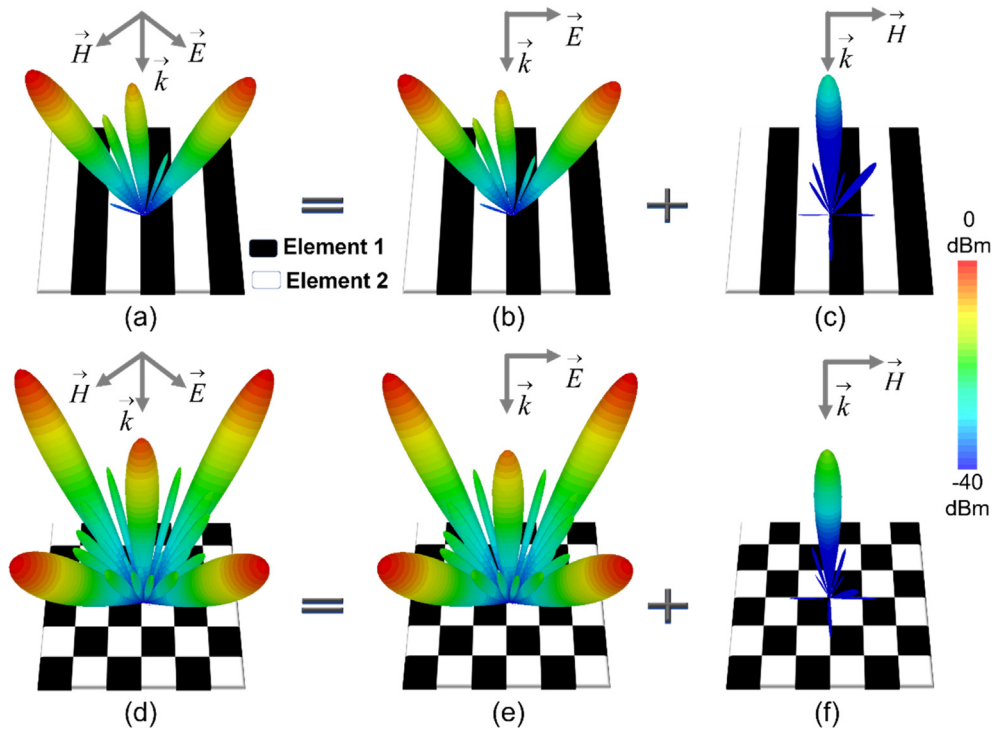
Fig. 5. Simulated 3D scattering patterns of the proposed meta-filter for linear-polarization decomposition and manipulation at 10 GHz: (a, d) illuminated with the 45° polarized incident waves; (b, e) TM component; (c, f) TE component.
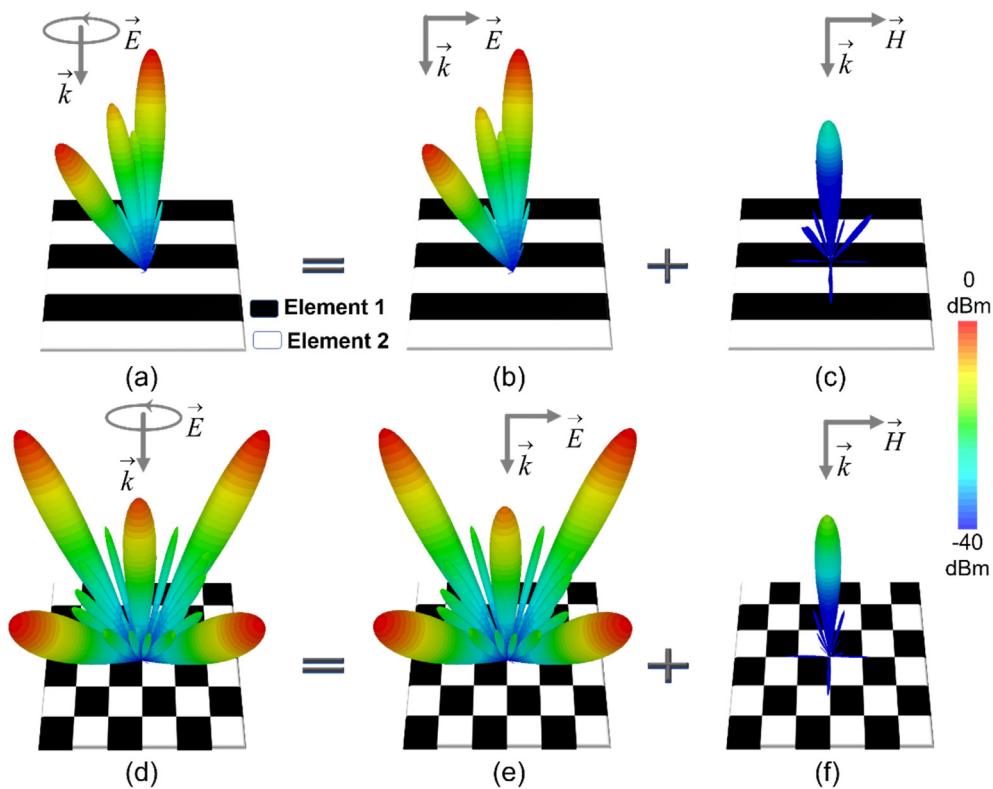

Fig. 6. Simulated 3D scattering patterns of the proposed meta-filter for circular-polarization decomposition and manipulation at 10 GHz: (a, d) illuminated with left circular-polarized incident waves; (b, e) TM component; (c, f) TE component.

deformation (Fig. 5(b)). In the meanwhile, due to the remarkable absorption ability of the typical meta-atoms (Fig. 1(c)), a sum beam is observed with ultra-low energy (Fig. 5(c)). In the other example, the same phenomena can be observed in Fig. 5(d − f) despite the different chess-board-like aperture. Thus, based on our proposed strategy, a classical four-beam splitting can be decomposed into

a same-shaped TM part and a small pen-shaped single beam in the TE mode.

Next, a more universal case is presented in Fig. 6 to demonstrate the ability of the proposed method to break the circular polarization and control the needed part. When illuminated by a left circular-polarized normal incident wave, the TM component (Fig. 6(b) and 6(e)) can be extracted from the total 3D scattering patterns (Fig. 6(a) and 6(d)) and flexibly manipulated based on the array antenna theory [51]. Note that since the unit cell distribution across the meta-filter is rotated by 90°, the simulated two-beam patterns (Fig. 6(a − b)) are orthogonal with those in Fig. 5(a − b). In addition, by comparing the second and third columns of Figs. 5 and 6, the high isolation between TM and TE modes can be achieved, proving that our strategy can pave a novel way to realize polarization purification and manipulation.

3. Experimental section

3.1. Fabrication and characterization of graphene films with flexible sheet resistance

Graphene film can be fabricated by reducing the graphene oxide (GO) film. To achieve a film with high conductivity, the high-temperature annealing method [52] is usually adopted under an argon atmosphere to ensure maximum reduction. In this experiment, Film 1 with the sheet resistance of 0.03 ± 0.001 Ω/□ and a thickness of 25 μm, is assembled at 3000 ℃ for 2 h (left-side image of Fig. 7(b)). However, the sheet resistance of the fabricated graphene film cannot be tuned easily based on this method as its extent of reduction is not controllable.

To break this limitation, a chemistry method is put forward to flexibly adjust the reduction process. Ascorbic acid aqueous solution is selected as the reducing agent without inducing environmental pollution. To more accurately control the reduction degree, we determine the conductivity range by analyzing the effect of the concentration of the aqueous ascorbic acid solution

and the reduction time on the reduction procedure (Fig. 7(a)). The results indicate that arbitrary sheet-resistance values (from 15 Ω/□ to 700 Ω/□) of the synthesized graphene film can be successfully realized by choosing the appropriate concentration and reduction time. Thus, Film 2 is produced by reducing a GO film in an aqueous ascorbic acid solution (100 mg/mL) for 3 h (Fig. 7 (a)). The measured sheet resistance of the 13-μm Film 2 is 35 ± 1 Ω/□ (right-side image in Fig. 7(b)). (See **Supplementary Note S3 for a detailed description of the fabrication method for the reduced GO films**)

Film 1 and Film 2 are characterized based on their scanning electron microscopy (SEM) images (Fig. 7(b)), Raman spectra (Fig. 7(c)) and X-ray diffraction (XRD) spectra (Fig. 7(d)). In Film 1, a strong G' peak and weak D peak can be observed due to the high-quality graphitization (red line in Fig. 7(c)), while the strong D peak of Film 2 indicates more defects are present, leading to the decrease of the conductivity (olive-green line in Fig. 7(c)). In addition, it should be noted that the I_D/I_G of Film 1 (1.356) is much greater than that of Film 2 (0.051), indicating that Film 1 has more sp^2 carbon restoration and higher conductivity. This can be further demonstrated by the XRD spectra shown in Fig. 7(d). The full width at half maximum (FWHM) of Film 1 is much smaller than that of Film 2, indicating that Film 1 has a higher degree of reduction and better crystallinity after the high-temperature heat treatment. While the reduction degree of Film 2 is lower, thus lower degree of sp^2 hybridization.

3.2. Fabrication and measurement of the sample

To verify the correctness of our design, the samples (192 mm × 192 mm) for Case 1 (**Supplementary Fig. S3(b)**) and Case 2 (first example, **Supplementary Fig. S3(c)**) are fabricated based on the optimal structural parameters listed in **Supplementary Table S1** and the spatial distributions of the meta-atoms shown in Fig. 4(a − f) and 5(a − c), respectively. Details of the manufacturing process can be found in **Supplementary Note S4**. The practical polarization decomposition and control performance of
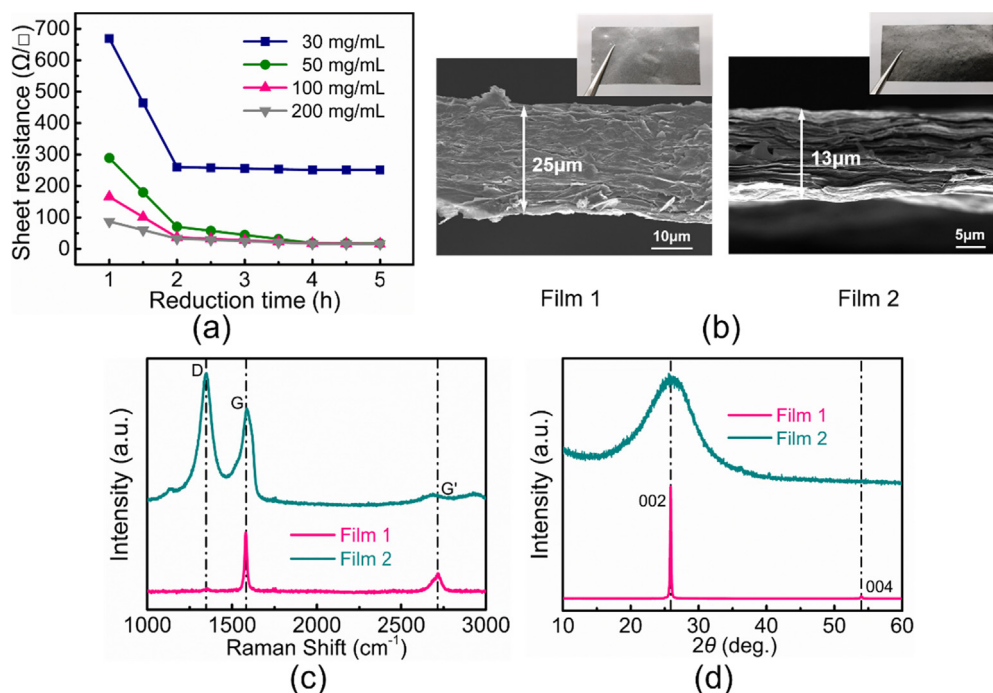

Fig. 7. (a) Sheet resistance of the graphene film versus reduction time using different ascorbic acid concentrations. SEM image (b, insets: corresponding photographs), Raman spectra (c), and XRD spectra (d) of the fabricated Film 1 and Film 2.
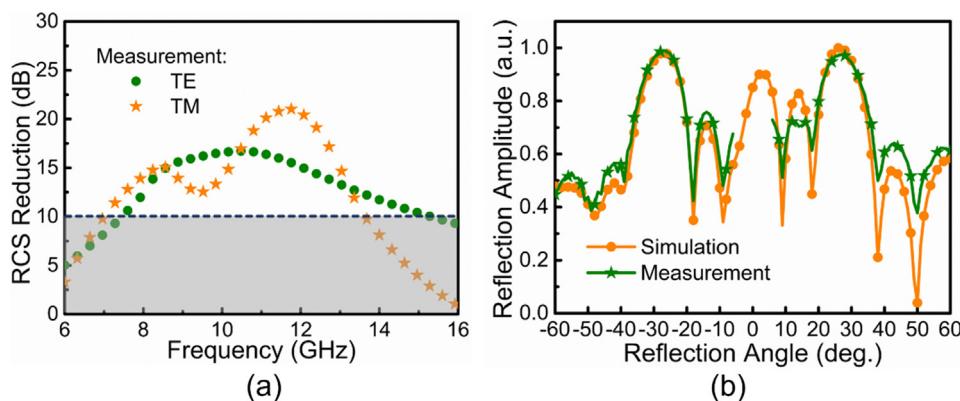
Fig. 8. (a) Measured broadband RCS reduction performance of Case 1. (b) Measured TM component 2D scattering patterns of Case 2 at 10 GHz.

the samples are measured using the arch method in an anechoic chamber. In the investigation region from 6 to 16 GHz, the experiment is conducted on a vector network analyzer (VNA, Agilent Technology N5247A to 40 GHz). The measurement environment and custom-built setup are presented in **Supplementary Fig. S3 (a)**. (See **Supplementary Note S5 for a detailed description of the measurement procedures**)

4. Result and discussion

Concerning the sample (**Supplementary Fig. S3(b)**) in Case 1, the anisotropic performance is measured. Under normal TE plane wave, the measured RCS reduction performance (Fig. 8(a)) of the sample is obtained from 6 GHz to 16 GHz, showing that the scattering of gigahertz waves is fully controllable as desired. As a result of the manufactural error and the inaccuracy of sheet resistance, a slight red shifting in the operating frequency band can be observed by comparing Fig. 8(a) with Fig. 4(j), which has no effect on the overall performance. In the meantime, for the TM case, the meta-filter shows excellent broadband properties, with RCS reduction greater than 10 dB from 6.7 GHz to 14 GHz. Discrepancies compared with the simulated result (Fig. 4(k)) can be mostly attributed to inaccuracies in the multilayer alignment and measurement errors. Even so, both the TE and TM cases demonstrate good correspondence with the previous predictions (Fig. 4(j − k)).

With regard to the sample (**Supplementary Fig. S3(c)**) in Case 2, the TM part of the overall 2D scattering patterns at 10 GHz is revealed in Fig. 8(b), when illuminated with the linear-polarized incident plane wave, of which the E-field occurs along the diagonal line (Fig. 5(a) and 5(d)). Two symmetric beams can be observed in Fig. 8(b) based on Fig. 5(b). And the deflected angles can be successfully predicted using the equation [50]: $\theta = \sin^{-1}(\lambda/\Gamma)$, where λ is the free-space wavelength at 10 GHz (30 mm), and Γ is the periodicity of the minimum repeat structure (64 mm). It is obvious that the simulated and the measured bending angles (Fig. 8(b)) agree well with the calculated one of ± 27.95°. Besides, the measured 2D spatial patterns are consistent with the simulated one in addition to the little discrepancy at the side lobes (Fig. 8(b)). Note that due to the limitation of the test system, the scattering patterns from − 6° to 6° cannot be obtained.

5. Conclusion

In summary, a graphene-built meta-filter is innovatively promoted and investigated to carry out the treatment of useless polarization energy, as well as feasibly control of other components. Our finding reveals that the anisotropic meta-filter enables a strong

ability to independently control EM waves under different polarizations. Incident TE waves are absorbed by middle-layered SRRs. However, when exposed to TM waves, the bi-functional meta-filter can implement flexible spatial patterns with almost no reflection loss. The abovementioned anisotropic performance can be simultaneously achieved in the working frequency band from 8 GHz to 14 GHz. Importantly, our strategy also opens another door to decomposing arbitrary incoming polarized states such as linear-, circular-, and even elliptical-polarizations. In addition, taking advantage of the home-made graphene film, we anticipate that our design can contribute to resolving recent global EM issues in extreme natural environment, severely threatening electronic device operations and thus human life.

Declaration of Competing Interest

The authors declare that they have no known competing financial interests or personal relationships that could have appeared to influence the work reported in this paper.

Appendix A. Supplementary data

Supplementary data to this article can be found online at https://doi.org/10.1016/j.matdes.2021.109768.

References

[1] A.N. Uwaechia, N.M. Mahyuddin, A Comprehensive Survey on Millimeter Wave Communications for Fifth-Generation Wireless Networks: Feasibility and Challenges, IEEE Access 8 (2020) 62367–62414.

[2] M.I. Hayee, M.C. Cardakli, A.B. Sahin, A.E. Willner, Doubling of bandwidth utilization using two orthogonal polarizations and power unbalancing in a polarization-division-multiplexing scheme, IEEE Photon. Technol. Lett. 13 (2001) 881–883.

[3] B.Z. Katsenelenbaum, High-Frequency Electrodynamics, John Wiley & Sons, 2006.

[4] J.A. Kong, Electromagnetic Wave Theory, Cambridge, EMW Publishing, MA, 2005.

[5] Y. Jung, H. Jung, H. Choi, H. Lee, Polarization Selective Color Filter Based on Plasmonic Nanograting Embedded Etalon Structures, Nano Lett. 20 (2020) 6344–6350.

[6] M.M.J. Treacy, Dynamical diffraction explanation of the anomalous transmission of light through metallic gratings, Phys. Rev. B 66 (2002) 195105.

[7] Y. Liu, Q. Guo, H. Liu, C. Liu, K. Song, B. Yang, Q. Hou, X. Zhao, S. Zhang, M.N. Cía, Circular-polarization-selective transmission induced by spin-orbit coupling in a helical tape waveguide, Phys. Rev. Applied 9 (2018) 054033.

[8] J.J. Cadusch, T.D. James, A.D. Assl, T.J. Davis, A. Roberts, A chiral plasmonic metasurface circular polarization filter, IEEE Photon. Technol. Lett. 26 (2014) 2357–2360.

[9] M.M. Rahman, A. Khaleque, M.T. Rahman, F. Rabbi, Gold-coated photonic crystal fiber based polarization filter for dual communication windows, Opt. Commun. 461 (2020) 125293.

[10] J. Xue, S. Li, Y. Xiao, W. Qin, X. Xin, X. Zhu, Polarization filter characters of the gold-coated and the liquid filled photonic crystal fiber based on surface plasmon resonance, Opt. Express 21 (2013) 13733–13740.

[11] W. Tang, H. Zhang, H. Ma, W. Jiang, T.J. Cui, Concept, theory, design, and applications of spoof surface plasmon polaritons at microwave frequencies, Adv. Opt. Mater. 7 (2019) 1800421.

[12] L. Jidi, X. Cao, J. Gao, S. Li, H. Yang, T. Li, Excitation of odd-mode spoof surface plasmon polaritons and its application on low-pass filters, Appl. Phys. Express 13 (2020) 084004.

[13] Y.J. Guo, K.D. Xu, X. Deng, X. Cheng, Q. Chen, Millimeter-wave on-chip bandpass filter based on spoof surface plasmon polaritons, IEEE Electron Device Lett. 41 (2020) 1165–1168.

[14] N.F. Yu, F. Capasso, Flat optics with designer metasurfaces, Nature Mater. 13 (2014) 139–150.

[15] N.M. Estakhri, A. Alù, Wave-front Transformation with Gradient Metasurfaces, Phys. Rev. X 6 (2016) 041008.

[16] T.J. Cui, Microwave metamaterials, Natl. Sci. Rev. 5 (2018) 134–136.

[17] C. Zhang, W.K. Cao, L.T. Wu, J.C. Ke, Y. Jing, T.J. Cui, Q. Cheng, A reconfigurable active acoustic metalens, Appl. Phys. Lett. 118 (2021) 133502.

[18] H. Ren, X. Fang, J. Jang, J. Bürger, J. Rho, S.A. Maier, Complex-amplitude metasurface-based orbital angular momentum holography in momentum space, Nat. Nanotechnol. 15 (2020) 948–955.

[19] K. Chen, G. Ding, G. Hu, Z. Jin, J. Zhao, Y. Feng, T. Jiang, A. Alù, C. Qiu, Directional janus metasurface, Adv. Mater. 32 (2020) 1906352.

[20] H.T. Zhou, W.X. Fu, Y.F. Wang, Y.S. Wang, V. Laude, C. Zhang, Ultra-broadband passive acoustic metasurface for wide-angle carpet cloaking, Mater. Des. 199 (2021) 109414.

[21] X. Xu, C. Wang, W. Shou, Z. Du, Y. Chen, B. Li, W. Matusik, N. Hussein, G. Huang, Physical Realization of Elastic Cloaking with a Polar Material, Phys. Rev. Lett. 124 (2020) 114301.

[22] E.E. Narimanov, A.V. Kildishev, Optical black hole: Broadband omnidirectional light absorber, Appl. Phys. Lett. 95 (2009) 041106.

[23] Q. Bai, J. Chen, N.H. Shen, C. Cheng, H.T. Wang, Controllable optical black hole in left-handed materials, Opt. Express 18 (2010) 2106–2115.

[24] Z. Zhang, J. Wang, R. Zhu, Y. Jia, T. Liu, M. Yan, J. Jiang, Y. Li, Y. Meng, S. Qu, Multifunctional full-space metasurface controlled by frequency, polarization and incidence angle, Opt. Express 29 (2021) 7544–7557.

[25] X. Ding, F. Monticone, K. Zhang, L. Zhang, D. Gao, S.N. Burokur, A. Lustrac, Q. Wu, C. Qiu, A. Alù, Ultrathin Pancharatnam-Berry metasurface with maximal cross-polarization efficiency, Adv. Mater. 27 (2015) 1195–1200.

[26] L. Shao, M. Premaratne, W. Zhu, Dual-functional coding metasurfaces made of anisotropic all-dielectric resonators, IEEE Access 7 (2019) 45716–45722.

[27] T.J. Cui, R.Y. Wu, W. Wu, C.B. Shi, Y.B. Li, Large-scale transmission-type multifunctional anisotropic coding metasurfaces in millimeter-wave frequencies, J. Phys. D 50 (2017) 404002.

[28] J.B.O.D. Araújo, G.L. Siqueira, E. Kemptner, M. Weber, C. Junqueira, M.M. Mosso, An ultrathin and ultrawideband metamaterial absorber and an equivalent-circuit parameter retrieval method, IEEE Trans. Antennas Propag. 68 (2020) 3739–3746.

[29] C. Du, D. Zhou, H.H. Guo, Y.Q. Pang, H.Y. Shi, W.F. Liu, J.Z. Su, C. Singh, S. Trukhanov, A. Trukhanov, L. Panina, Z. Xu, An ultra-broadband terahertz metamaterial coherent absorber using multilayer electric ring resonator structures based on anti-reflection coating, Nanoscale 12 (2020) 9769–9775.

[30] Z. Zhang, M. Huang, Y. Chen, S.W. Qu, J. Hu, S. Yang, In-Band Scattering Control of Ultra-Wideband Tightly Coupled Dipole Arrays Based on Polarization-Selective Metamaterial Absorber, IEEE Trans. Antennas Propag. 68 (2020) 7927–7936.

[31] F. Ding, Y. Cui, X. Ge, Y. Jin, S. He, Ultra-broadband microwave metamaterial absorber, Appl. Phys. Lett. 100 (2012) 103506.

[32] D. Hu, J. Cao, W. Li, C. Zhang, T. Wu, Q. Li, Z. Chen, Y. Wang, J. Guan, Optically Transparent Broadband Microwave Absorption Metamaterial by Standing-up Closed-Ring Resonators, Adv. Opt. Mater. 5 (2017) 1700109.

[33] W. Li, J. Wei, W. Wang, D. Hua, Y. Li, J. Guan, Ferrite-based metamaterial microwave absorber with absorption frequency magnetically tunable in a wide range, Mater. Des. 110 (2016) 27–34.

[34] S. Liu, H. Chen, T.J. Cui, A broadband terahertz absorber using multi-layer stacked bars, Appl. Phys. Lett. 106 (2015) 151601.

[35] M. Lawrence, D.R. Barton III, J. Dixon, J.H. Song, J. Groep, M.L. Brongersma, J.A. Dionne, High quality factor phase gradient metasurfaces, Nat. Nanotechnol. 15 (2020) 956–961.

[36] D. Lin, P. Fan, E. Hasman, M.L. Brongersma, Dielectric gradient metasurface optical elements, Science 345 (2014) 298–302.

[37] M. Mohsenizadeh, F. Gasbarri, M. Munther, A. Beheshti, K. Davami, Additively-manufactured lightweight Metamaterials for energy absorption, Mater. Des. 139 (2018) 521–530.

[38] Z. Zhou, K. Chen, B. Zhu, J. Zhao, Y. Feng, Y. Li, Ultra-wideband microwave absorption by design and optimization of metasurface salisbury screen, IEEE Access 6 (2018) 26843–26853.

[39] T. Wang, P. Wang, Y. Wang, L. Qiao, A broadband far-field microwave absorber with a sandwich structure, Mater. Des. 95 (2016) 486–489.

[40] P. Li, Z. Wang, R. Song, W. Qian, P. Wen, Z. Yang, D. He, Customizable fabrication for auxetic graphene assembled macrofilms with high conductivity and flexibility, Carbon 162 (2020) 545–551.

[41] R.G. Song, Q.L. Wang, B.Y. Mao, Z. Wang, D.L. Tang, B. Zhang, J.W. Zhang, C.G. Liu, D.P. He, Z. Wu, S.C. Mu, Flexible graphite films with high conductivity for radio-frequency antennas, Carbon 130 (2018) 164.

[42] H. Lv, Z. Yang, B. Liu, G. Wu, Z. Lou, B. Fei, R. Wu, A flexible electromagnetic wave-electricity harvester, Nat. Commun. 12 (2021) 834.

[43] W. Zhou, C. Liu, R. Song, X. Zeng, B. Li, W. Xia, J. Zhang, G. Huang, Z.P. Wu, D. He, Flexible radiofrequency filters based on highly conductive graphene assembly films, Appl. Phys. Lett. 114 (2019) 113503.

[44] K. Pan, Y. Fan, T. Leng, J. Li, Z. Xin, J. Zhang, L. Hao, J. Gallop, K.S. Novoselov, Z. Hu, Sustainable production of highly conductive multilayer graphene ink for wireless connectivity and IoT applications, Nat. Commun. 9 (2018) 5197.

[45] A. Scidà, S. Haque, E. Treossi, A. Robinson, S. Smerzi, S. Ravesi, S. Borini, V. Palermo, Application of graphene-based flexible antennas in consumer electronic devices, Mater. Today 21 (2018) 223–230.

[46] C. Zhang, C.G. Ji, Y.B. Park, L.J. Guo, Thin-Metal-Film-Based Transparent Conductors: Material Preparation, Optical Design, and Device Applications, Adv. Opt. Mater. 9 (2020) 2001298.

[47] Q. Ma, T.J. Cui, Information Metamaterials: bridging the physical world and digital world, PhotoniX 1 (2020) 1.

[48] C. Caloz, T. Itoh Electromagnetic Metamaterials: Transmission Line Theory and Microwave Applications Wiley (2005).

[49] D.M. Pozar, Microwave Engineering, John Wiley & Sons, Toronto (1998).

[50] N.F. Yu, P. Genevet, M.A. Kats, F. Aieta, J.P. Tetienne, F. Capasso, Z. Gaburro, Light Propagation with Phase Discontinuities: Generalized Laws of Reflection and Refraction, Science 334 (2011) 333–337.

[51] C.A. Balanis, Antenna Theory: Analysis and Design, John Wiley & Sons, 2016.

[52] S.F. Pei, H.M. Cheng, The reduction of graphene oxide, Carbon 50 (2012) 3210–3228.